Int. J. Electrochem. Sci., 16 **(2021)** Article ID: 210462, doi: 10.20964/2021.04.04

International Journal of
ELECTROCHEMICAL
SCIENCE
www.electrochemsci.org

Hierarchical $NiCo_2O_4$@$NiCo_2O_4$ Nanoflake Arrays Supported on Ni Foam as High-performance Electrodes for Supercapacitors

Tingting Liu[1,*], *Yujie Wei*[2], *Xiangcheng Chen*[2], *Xinyong Yu*[2], *Ling Chen*[2,3,*]

[1] Northeast Petroleum University Qinhuangdao, Qinhuangdao 066004, China
[2] Hebei Key Laboratory of Applied Chemistry, College of Environmental and Chemical Engineering, Yanshan University, Qinhuangdao, Hebei 066004, China
[3] Hebei Key Laboratory of heavy metal deep-remediation in water and resource reuse, College of Environmental and Chemical Engineering, Yanshan University, Qinhuangdao, Hebei 066004, China
[*]E-mail: 2008little@163.com, hhchen@ysu.edu.cn

Received: 6 November 2020 / *Accepted:* 9 January 2021 / *Published:* 28 February 2021

A facile strategy for the stepwise preparation of a $NiCo_2O_4$ nanosheet array on a nickel foam skeleton was developed by a hydrothermal-calcination method. Under optimum process conditions, the $NiCo_2O_4$@$NiCo_2O_4$ materials supported on $NiCo_2O_4$ nanoflakes displayed different performances than bare $NiCo_2O_4$ nanosheet arrays according to experimental characterization and electrochemical studies and were grown in situ on nickel foam. The $NiCo_2O_4$ nanoflake material, used as the electrode of the supercapacitor, exhibited a multilevel mesoporous nanostructure that had a narrow pore size (3.18 nm) and wide pore size (6.22 nm). In addition, the specific surface area (SSA, 1.84 m^2g^{-1}) and average pore size (13 nm) were acquired by calculations, and this material showed a relatively high specific capacitance (C_s, 840 Fg^{-1}) when the current density was $1Ag^{-1}$, and a rate capability of 86.67% from 1 to 15 Ag^{-1} and the capacitance could maintain 93% of the initial value after 5000 charge-discharge cycles. The $NiCo_2O_4$@$NiCo_2O_4$ nanostructures provided effective electron pathways and a relatively large electroactive surface area, and narrow pore sizes were observed at 2.46 nm and 3.48 nm, while a wide pore size was observed at 5.53 nm. The SSA was improved to 8.64 m^2g^{-1}, and the average pore diameter was distributed at 11 nm. Accordingly, a remarkable electrochemical performance demonstrated that the C_s of 1036 Fg^{-1} was obtained at a current density of 1 Ag^{-1}, and the rate capability reached 69.59% as the current density increased from 1 to 15 Ag^{-1}.Excellent capacitance retention was retained at 92.5% after 5000 cycles, while the coulombic efficiency was maintained at 100%.

Keywords: $NiCo_2O_4$, Hierarchical structure, Hydrothermal calcination method, Supercapacitors

1. INTRODUCTION

Due to the rapid consumption of fossil energy and the need for sustainable clean energy, scientific communities have paid great attention to the improvement of materials and efficient methods for the optimum utilization of renewable and clean energies [1-3]. The supply of energy has fallen short of demand in the past few years. Consequently, the design of efficient & alternative energy storage devices is urgently needed. Supercapacitors with higher energy storage than batteries and conventional capacitors are supposed to be more promising in terms of the many kinds of energy storage systems [4-9]. In the past few years, they have attracted more attention owing to their particular advantages of a long cycling life, rapid recharging capability and high reliability [10]. These unique features are supposed to make supercapacitors widely applicable in electric vehicles, backup energy systems and miniature electronic devices [11-14]. Electrode materials, which are a key component influencing the electrochemical properties of a supercapacitor, are designed to fabricate high-performance supercapacitors, and they are typically divided into three main types: carbon materials, transition metal oxides (TMO) [15] and conducting polymers [16]. Carbon materials, benefiting from a large SSA, chemical stability, good electrical conductivity, and low cost of production, are regarded as desired materials for supercapacitor electrodes; however, the intrinsic deficiency of this material (poor C_s) is inescapable. Conducting polymers have slightly higher C_s and better electrical conductivity than carbon materials, but their cycling performance is particularly inferior, originating from the drastic expansion of their volume when tested in the charging-discharging processes [17, 18]. For the comparison of the two types of materials mentioned above, transition metal oxides possess multiple oxidation states, which is beneficial to rapid Faraday reactions, leading to a much higher specific capacitance [19-21]. Overall, the low electronic conductivity of these transition metal oxides makes it difficult for them to maintain their excellent properties especially their high rate capability unless they are combined with other good conductive materials [22].

Previous reports have proven that the complex process of combining active materials with binders can be solved when active materials directly grow on nickel foam [23-25] . In these cases, the nickel foam can significantly increase the contact of the active substance with the electrolyte, improve porosity, shorten the distance of electron transmission and provide more active materials without any auxiliary components [26]. Every structure of active materials grown on nickel foam are closely contacts with current collectors where numerous open spaces between neighbor microstructures exist. This favors facilitating electrolyte penetration and rapid charge exchange [27-29]. Among these transition metal oxides, $NiCo_2O_4$ is expected to complement or replace electrode materials such as NiO[30], Co_3O_4[31, 32] and MnO_2[33, 34] in energy storage systems due to its environmentally friendliness, low cost and outstanding electrochemical performance [8, 31, 33, 35]. Various nanostructures of $NiCo_2O_4$ materials, including nanoparticles [36], nanowires [37-39], nanoflowers[40], nanosheet arrays [11], and nanoneedle arrays [41] have been researched in the past years. The electrochemical performance of $NiCo_2O_4$ has a close relationship with the morphology [42-44]. The directional stacking arrangement of electrode materials makes the active materials obtain adjustable free pores, which greatly improves the utilization rate of active substances. Moreover, the morphology of manufacturing materials has a great effect on the ion transfer rate and charge storage

capacity. Therefore, synthesizing materials with excellent morphology has been desired [12]. In a large number of studies, the substrate structure grown on nickel foam in situ is mostly nanoneedles. However, when a nanoneedle grows, it will have a thick bottom and a thin top. After a long charging and discharging cycle, mechanical expansion and destruction of the original structure easily occur, causing irreversible effects on the materials. Compared with one-dimensional nanoneedles, two-dimensional nanosheets have appropriate and uniform thickness and a high surface to volume ratio and are more suitable for secondary growth [15, 45, 46]. In addition, the novel flake nanostructure can effectively prevent flakes from accumulating, expose its active surface as much as possible, and further enhance electrochemical performance [16].

In this work, we designed a $NiCo_2O_4$ nanosheet on nickel foam as an electrode material under the optimum processing conditions, by the hydrothermal calcination method. The prepared $NiCo_2O_4$ nanosheets with relatively large specific surface area and an ample porous structure are superior in terms of electrochemical performance. On this basis, one novel $NiCo_2O_4$@$NiCo_2O_4$ nanomaterial used as an electrode is fabricated by a secondary hydrothermal calcination method on the substrate of $NiCo_2O_4$ nanosheets. This electrode demonstrates prominent electrochemical performance, such as high C_s and excellent cycling properties. Owing to efficient ion and electron transfer, abundant active sites and excellent strain accommodation, this nanoflake array has the potential to be applied to energy storage systems.

2. EXPERIMENTAL

2.1 Preparation of $NiCo_2O_4$ and $NiCo_2O_4$@$NiCo_2O_4$ nanoflake arrays

Before synthesis, pretreatment of nickel foam is required to eliminate the oxide layer and organic matter on the surface. Specifically, the nickel foams were etched in 3M dilute hydrochloric acid for 10 min and washed with acetone for another 20 min. Then, deionized water and absolute alcohol were used to rinse completely for standby application. Hierarchical $NiCo_2O_4$ was fabricated by adopting a hydrothermal and calcination method. Typically, 0.44 g nickel nitrate hexahydrate and 0.44 g cobalt nitrate hexahydrate were dissolved in the solution formed by 20 ml deionized water and 20 ml alcohol and stirring for 30 min. After dissolving completely, 0.84 g $C_6H_{12}N_4$ was added while stirring, and then the solution was poured to a 100 ml Teflon-lined stainless steel autoclave and soon afterwards immersed in one piece of pretreated nickel foam. The reaction kettle was transferred to a drying oven for 4 h at 120 ℃. After cooling to room temperature naturally after the reaction, nickel foam was removed, washed repeatedly with anhydrous ethanol and deionized water and dried in a constant temperature drying oven for 6 h to obtain the precursor grown on the nickel foam. The obtained precursors were calcined in a muffle furnace at 300 ℃ for 3 h. The obtained $NiCo_2O_4$ flake arrays, regarded as substrates, were transferred to a Teflon-lined autoclave with a solution mixed with 0.22 g $Ni(NO_3)_2{\cdot}6H_2O$, 0.22 g $Co(NO_3)_2{\cdot}6H_2O$ and 0.42 g $C_6H_{12}N_4$ for 4 h at 100 ℃.After the same method was performed, the $NiCo_2O_4$@$NiCo_2O_4$ materials with smaller strips and pores were synthesized. The entire process is illustrated in Scheme 1.

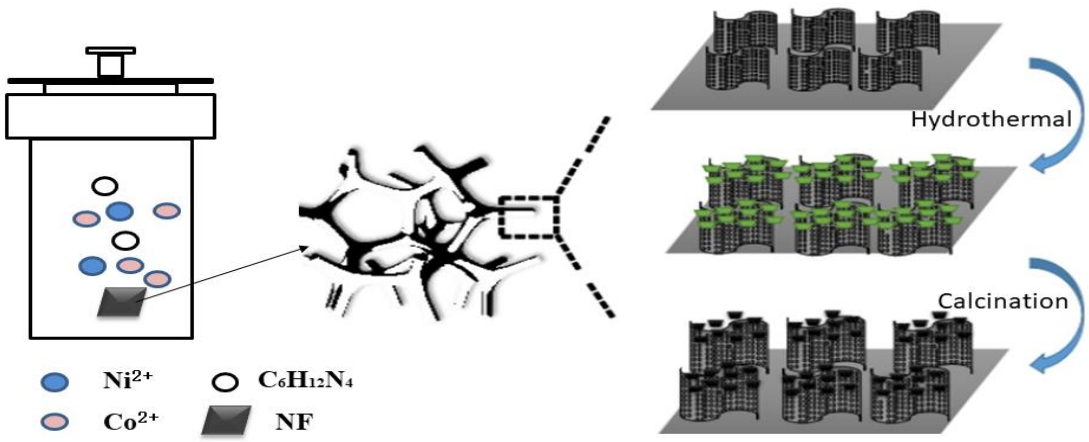

Scheme 1 Schematic of the preparation process used for the formation of $NiCo_2O_4$@$NiCo_2O_4$ materials

2.2 Characterizations

X-ray diffraction (XRD, Rigaku D-max-2500/PC) was adopted to detect the components and crystal forms of the prepared materials. The elemental composition was characterized by energy-dispersive spectroscopy (EDS, Genesis Apollo X/XL). The morphologies were determined through field emission scanning electron microscopy (SEM, KYKY-2800B) and transmission electron microscope (TEM, HT-7700). The Brunauer−Emmett−Teller (BET) specific surface areas were measured according to the nitrogen sorption isotherms with a Micromeritics Tristar II 3020 analyser, and the distributions of pore size were analysed with the help of adsorption branches according to the Barrett-Joyner-Halenda (BJH) model.

2.3 Electrochemical measurements

The electrochemical performances of the two different electrode materials were evaluated with a Chenhua CHI660E electrochemical workstation (Shanghai, China). The prepared electrode material, Hg/HgO electrode and platinum sheet (1 cm×1 cm) were used as the working electrode, reference electrode and auxiliary electrode, respectively. The three-electrode test device was assembled and finally equipped with 6 M KOH solution as the electrolyte. Then, the assembled device was immersed into the electrolyte for testing. Cyclic voltammetry (CV) was performed at 0.1-0.45 V. Electrochemical impedance spectroscopy (EIS) was performed in a certain frequency range of 10^{-2}~10^{5} Hz.Finally, the galvanostatic charge−discharge curves were measured on a CT-3008 tester.

3. RESULTS AND DISCUSSION

3.1 Material Characterization

Fig. 1a illustrates the XRD phase analysis of the $NiCo_2O_4$ precursor, $NiCo_2O_4$ and $NiCo_2O_4$@$NiCo_2O_4$ materials. In terms of the $NiCo_2O_4$ and $NiCo_2O_4$@$NiCo_2O_4$ samples, in addition to the Ni peaks, other obvious diffraction peaks can be observed at 18.9°, 31.1°, 36.7°, 44.6°, 59.1°and 64.9°, which correspond to the crystal planes of (111), (220), (311), (400), (511) and (440), respectively.

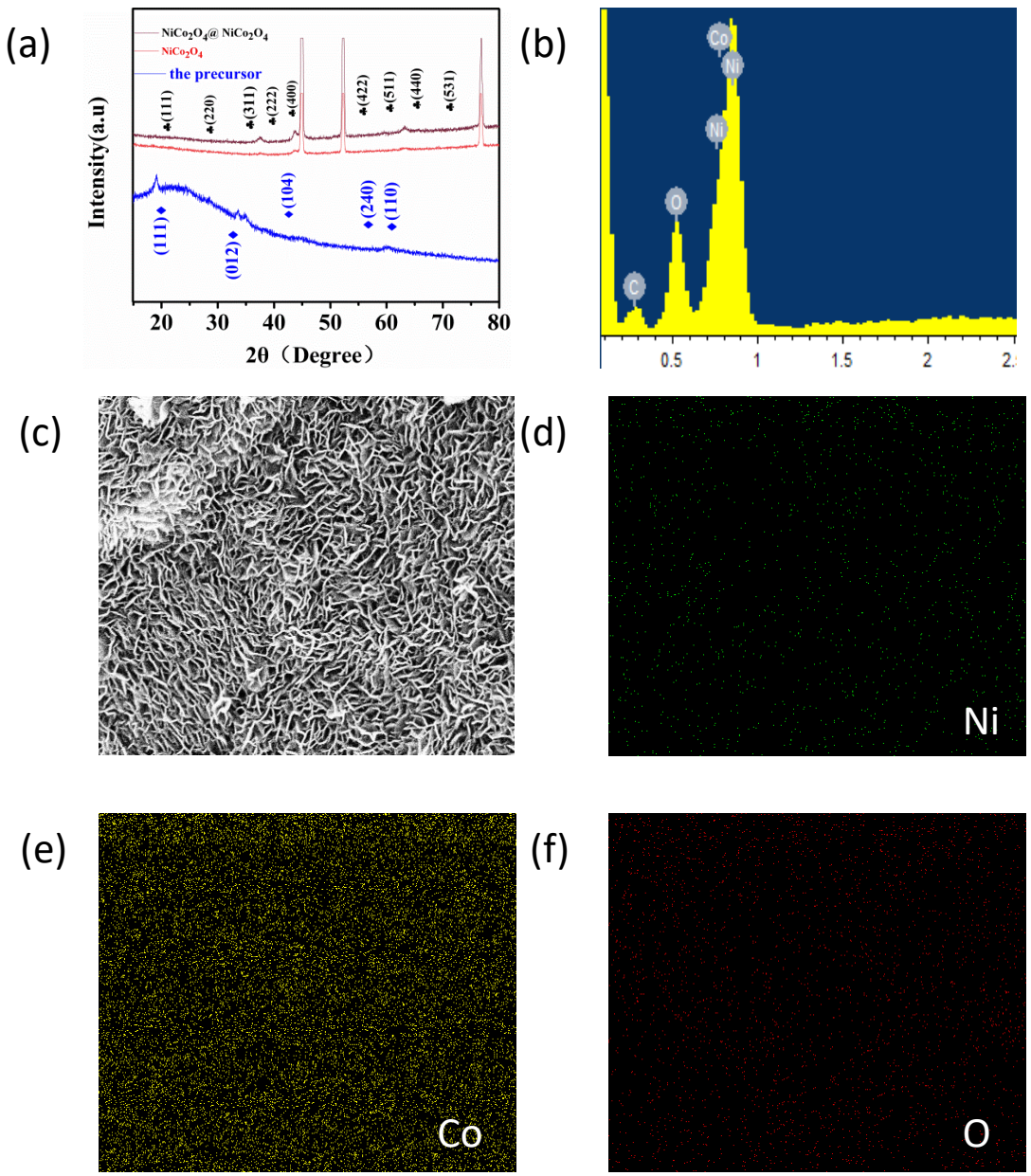

Figure 1. (a) XRD patterns of the sample, (b) EDS spectra of $NiCo_2O_4$@$NiCo_2O_4$, and (c-f) the corresponding EDS mapping.

The peaks are consistent with the standard card JCPDS no. 20-0781 card [47]. It can be concluded that the synthesized material growing on the nickel foam substrate is spinel nickel, cobaltite $NiCo_2O_4$. In addition, based on the EDS test, the elements in the composite sample (C from conductive tape) and elemental distribution are exhibited in Fig. 1b, proving the existence of Co and Ni and further confirming that the substance is $NiCo_2O_4$. Co, Ni and O are distributed quite evenly, as presented in Fig. 1 (c-f).

To determine the microstructure and morphology of the $NiCo_2O_4$ and $NiCo_2O_4$@$NiCo_2O_4$ materials, SEM and TEM tests were carried out. The SEM image from Fig. 2a, b demonstrates that the specific size of the $NiCo_2O_4$ material is approximately 1 μm, which is distributed uniformly, and the diameter of the spacer hole is approximately 500 nm. Fig. 2c, d shows that a large proportion of the nanoflake array becomes thicker, and after secondary growth, there are numerous smaller pieces without accumulation covering the surface of $NiCo_2O_4$, forming a highly porous architecture. The pores or voids between nanoflakes are supposed to provide an effective channel path for electrons and ions in the charge-discharge process.

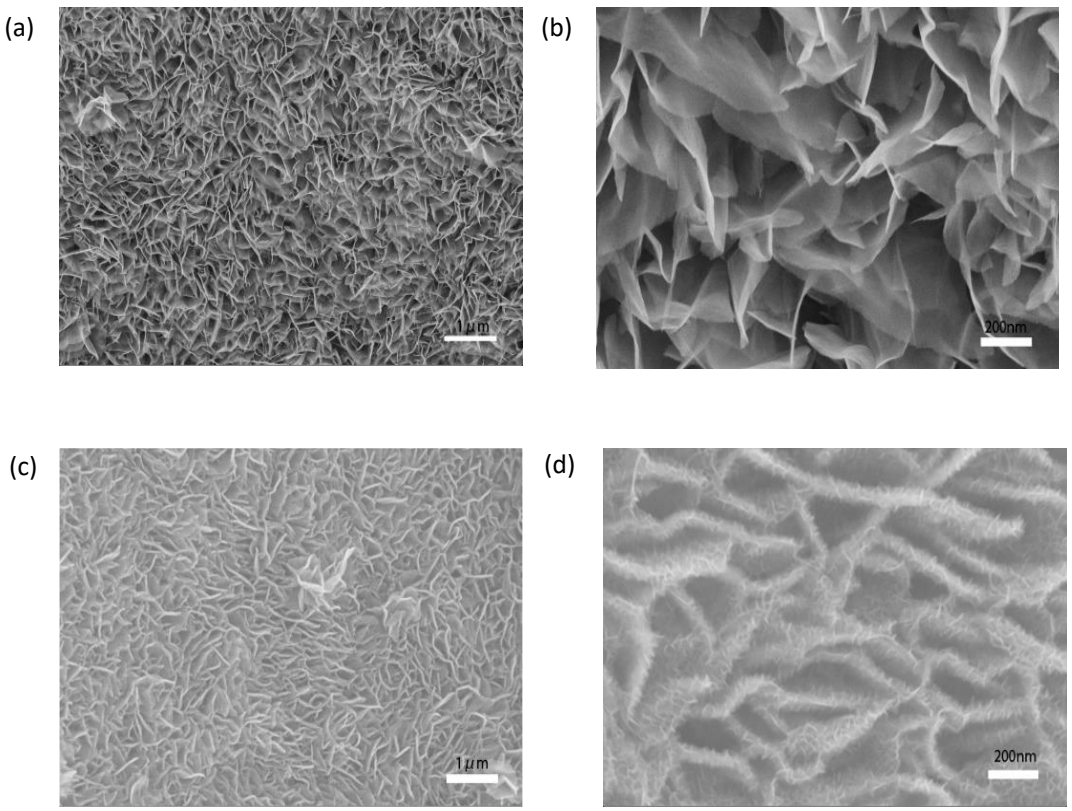

Figure 2. SEM images of $NiCo_2O_4$ (a), (b) and $NiCo_2O_4$@$NiCo_2O_4$(c), (d)

The TEM images of the $NiCo_2O_4$@$NiCo_2O_4$ and $NiCo_2O_4$ nanoflake arrays should be tested. As presented in Fig. 3a, the size of the sheet is approximately 1μm, and the surface is distributed uniformly. Fig. 3b illustrates that the lamellar surface has many mesoporous structures with sizes in the range of 5-10 nm. With the presence of these mesoporous structures, the specific surface area

apparently increases. Accordingly, the electrolyte and active substances have a closer connection, significantly enhancing the electrochemical performance of the samples.

Fig. 3c, d demonstrates that through secondary growth, the smaller nanoflakes are uniformly loaded on the large piece, leading to a nanostructure that has a large number of pores and corresponds to the SEM result.

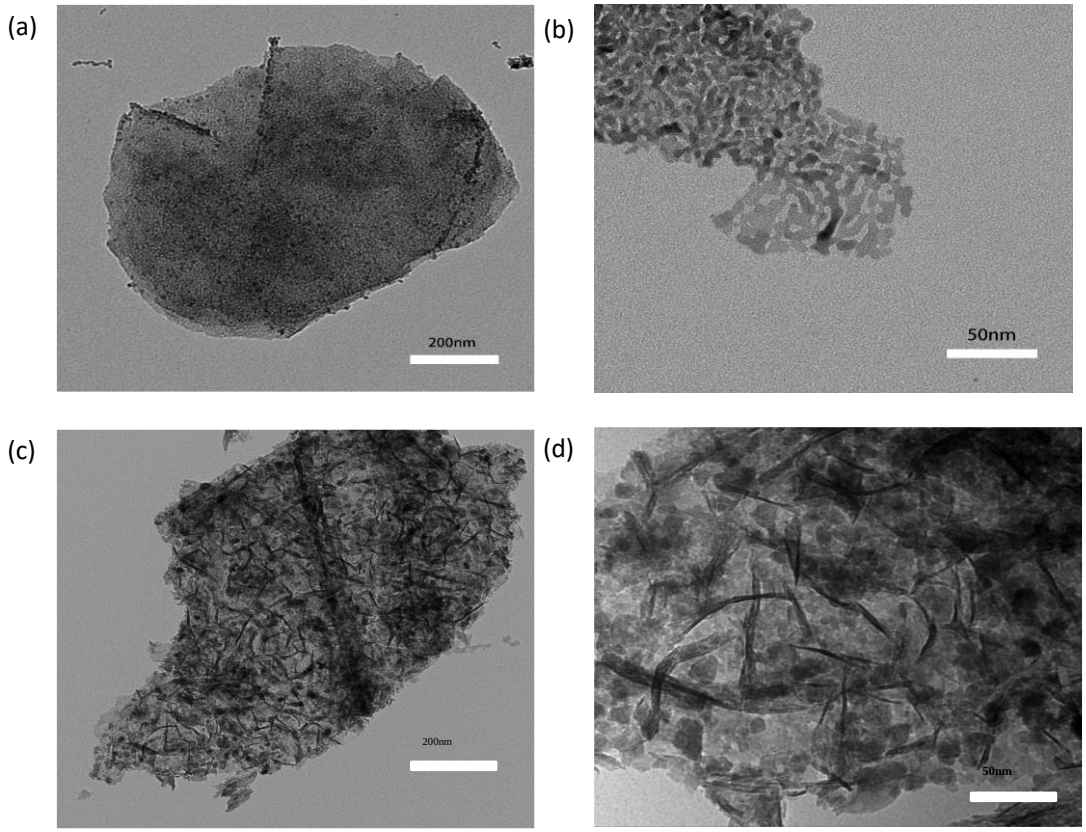

Figure 3. TEM images of $NiCo_2O_4$ (a-b) and $NiCo_2O_4$@$NiCo_2O_4$(c-d)

In addition, a BET test is adopted to further investigate the fabricated material microstructure, including the SSA and pore size. According to the nitrogen absorption/desorption curves in Fig. 4a obtained at 77 K, the N_2 isotherms are type IV and include a hysteresis loop [48], suggesting the existence of a mesoporous structure. The results showed that using small pieces for secondary growth further improved the specific surface area. It is obvious from the pore size distribution curves in Fig. 4b that the $NiCo_2O_4$ and $NiCo_2O_4$@$NiCo_2O_4$ materials showed different distributions of their pores. In detail, the sample of $NiCo_2O_4$ grown in situ on nickel foam had a flake morphology with a size of 0.8-1.4 μm, which showed a cross arrangement. This material exhibited a narrow pore size distribution at 3.18 nm and a wide pore size at approximately 6.22 nm, while the SSA was 1.84 m^2/g. With regard to the $NiCo_2O_4$@$NiCo_2O_4$ materials, narrow pore sizes were observed at 2.46 nm and 3.48 nm, while a wide pore size was observed at 5.53 nm. The SSA of this $NiCo_2O_4$@$NiCo_2O_4$ material was 8.64 m^2/g.

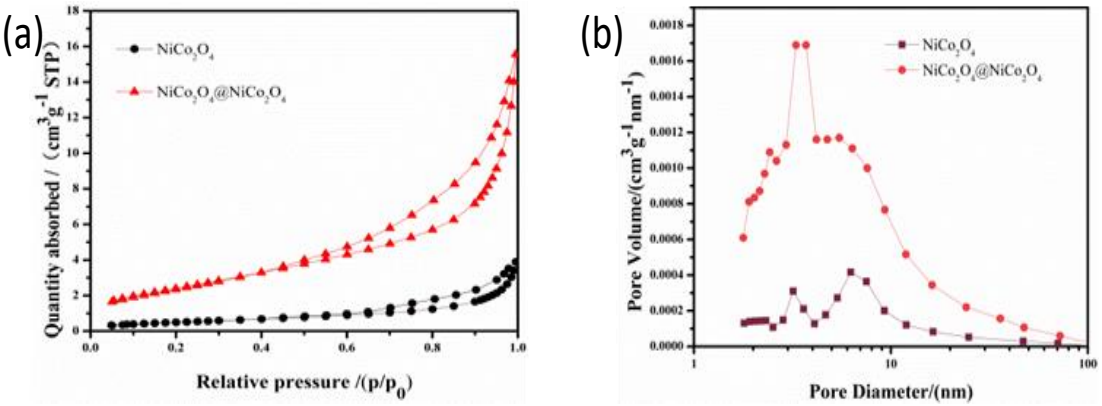

Figure 4. (a) Nitrogen adsorption/desorption curves, and (b) pore size distribution of $NiCo_2O_4$ and $NiCo_2O_4$@$NiCo_2O_4$.

3.2 Electrochemical Analysis

Representative CV curves of two different electrodes are illustrated with increasing scan rates. The characteristic CV curve is shown in Fig.5a, indicating that the $NiCo_2O_4$ materials exhibit prominent redox peak originating from the reversible faradaic redox reaction. The reduction and oxidation peaks are attributed to redox reactions of $NiCo_2O_4$, as represented in Equation (1)[45].

$NiCo_2O_4 + OH^- + 2H_2O \leftrightarrow NiOOH + 2CoOOH + H_2O + e^-$

$CoOOH + OH^- \leftrightarrow CoO_2 + H_2O + e^-$ （1）

The specific capacitance (*Cs*) of the electrode materials at different scan rates was calculated using Equation (2)[39].

$$C = \frac{\int Idv}{m\Delta V} \qquad (2)$$

where ΔV is the voltage range of the scan, v is the scan rate, I is the current density and m is the weight of the active substance, respectively. The calculated *Cs* values between 5 and 50 mV/s are 947, 938, 907, 875, 845 and 814 F/g respectively. In addition, the specific capacitance gradually decreases as presented in Fig. 5d.

Similarly, the similar CV curves in Fig. 5b are found at various scan rates for the $NiCo_2O_4$@$NiCo_2O_4$ nanoflake arrays. In addition, as the scan rates increase, the CV curves maintain approximately the same shapes, illustrating excellent stability and rapid faradaic redox reactions. It is because the unique nanostructure accelerates the rapid transmission of ions. The calculated specific capacitance of $NiCo_2O_4$@$NiCo_2O_4$ is 1080, 1013, 963, 902, 837 and 775 F/g with scan rates from 5 to 50 mV/s, respectively. Note that the *Cs* of the $NiCo_2O_4$@$NiCo_2O_4$ electrode is higher than that of $NiCo_2O_4$. Fig. 5c presents the CV curves of the two different electrode materials at a specific scan rate of 5 mV/s. Apparently, the area under of the CV curve of $NiCo_2O_4$@$NiCo_2O_4$ is much larger than that of $NiCo_2O_4$.

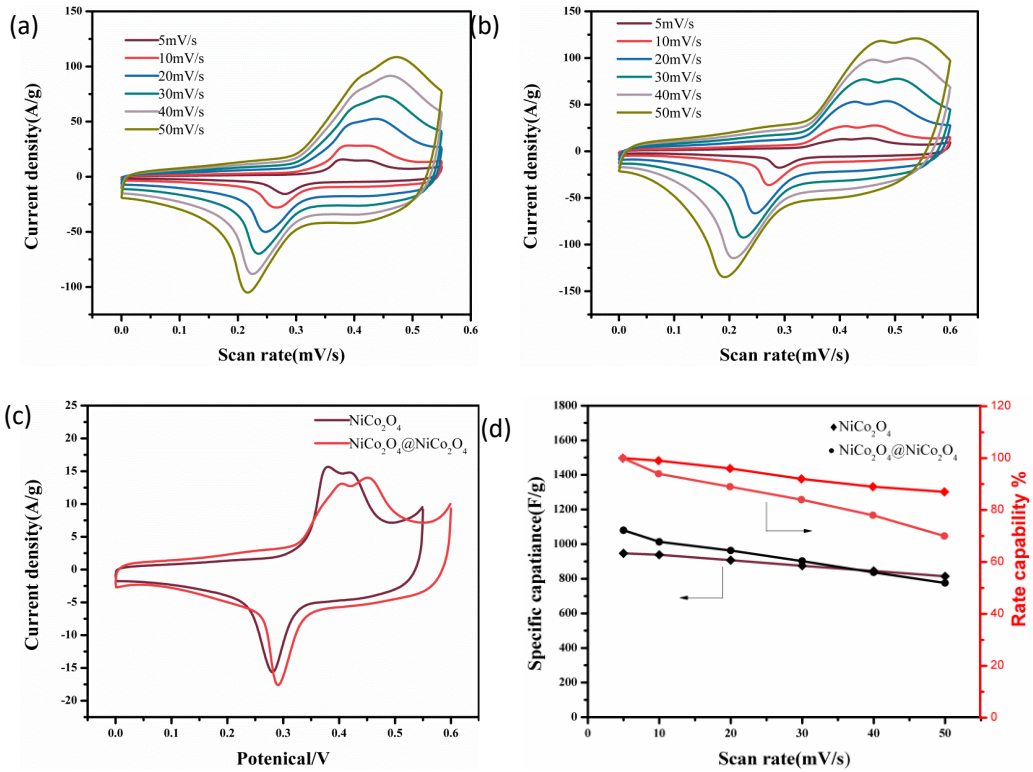

Figure 5. CV curves of $NiCo_2O_4$ (a) and $NiCo_2O_4$@$NiCo_2O_4$ (b) at different scan rates, (c) CV curves of $NiCo_2O_4$ and $NiCo_2O_4$@$NiCo_2O_4$ at a scan rate of 5 mV/s, and (d) variation in specific capacitance and capacity retention rate with scan rate as determined by cyclic voltammetry.

Galvanostatic charge−discharge measurements were further carried out to evaluate the capacitance of the two different electrodes in the voltage range of 0-0.5 V. The charge-discharge curves obtained for $NiCo_2O_4$ and $NiCo_2O_4$@$NiCo_2O_4$ at various current densities are given in Fig. 6a, b. The values of *Cs* are calculated using Equation (3):

$$C = \frac{I\Delta t}{m\Delta V} \qquad (3)$$

where *C*, *I*, *Δt*, *ΔV* and *m* are the specific capacitance, discharge current, discharge time, potential range during discharge, and mass of the active material in the electrode, respectively. Hence, as illustrated in Fig. 6d, the *Cs* values of $NiCo_2O_4$ are calculated as 837、793、767、756、736 and 728 F/g at discharge current densities of 1, 2, 3, 5, 10 and 15 A/g, respectively. The *Cs* values of $NiCo_2O_4$@$NiCo_2O_4$ electrode are calculated to be 1036、990、959、928、821 and 721 F/g respectively with increasing discharge current densities. However, the *Cs* of the $NiCo_2O_4$@$NiCo_2O_4$ material has not improved much, which can be attributed to the space limit of mass transfer. In this case, the typical pseudocapacitance characteristic is consistent with the cyclic voltammetry curve, proving the superiority of this material. Fig. 6c exhibits the discharge capacitance values for the $NiCo_2O_4$ and $NiCo_2O_4$@$NiCo_2O_4$ nanoflake arrays at 1 A/g, respectively. According to the different discharge times, it can be concluded that the latter delivers a higher specific capacitance.

This phenomenon should originate from the extra pseudocapacitance contributed by the outer $NiCo_2O_4$ on the surface of large piece. In addition, the mesoporous structure of nanoflake arrays with a larger surface area offers convenience for electrolyte permeation into the electrode inner region, improving the utilization of active substances and shortening the transportation/ ion diffusion paths for electrons and ions.

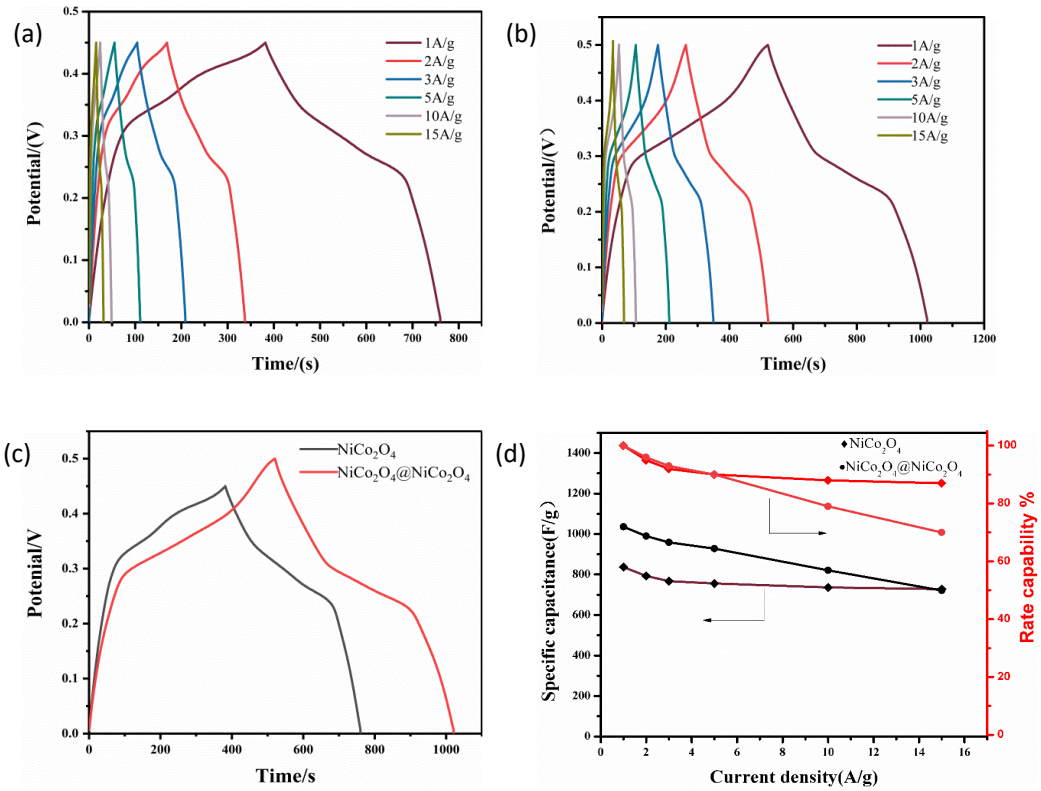

Figure 6. Galvanostatic charge–discharge graphs of $NiCo_2O_4$ (a) and $NiCo_2O_4$@$NiCo_2O_4$ (b) at different current densities, galvanostatic charge–discharge curves of $NiCo_2O_4$ and $NiCo_2O_4$@$NiCo_2O_4$ at 1 A/g, and (d) variation in specific capacitance and capacity retention rate with current density

Electrochemical impedance spectra (EIS) tests are used to research the charge transfer and diffusion process of ions in terms of the electrodes and electrolyte. Fig. 7a demonstrates the Nyquist plots of the $NiCo_2O_4$ and $NiCo_2O_4$@$NiCo_2O_4$ electrode materials. The enlarged impedance plot from the inset shows that the total resistance of the materials in the high-frequency area consists of the active substance, electrolyte and contact resistance. The values of the two kinds of electrolyte diffusion impedances determined by the slope of the straight line at the low frequency are nearly equal. From the inset, the hierarchical $NiCo_2O_4$@$NiCo_2O_4$ electrode delivers a much smaller internal resistance than the bare $NiCo_2O_4$ electrode. Based on the results, the effect of low electron-transfer resistance and fast ion diffusion enhances the electrochemical performance of the nanoflake arrays.

The cycling property, another factor affecting the practical application of electrode materials in terms of supercapacitors, is similarly estimated by repeated charging and discharging process at a current density of 10 A/g. Therein, the coulombic efficiency and retention rate of the materials are calculated. It is clearly noticed that the capacitance of $NiCo_2O_4$@$NiCo_2O_4$ electrode can be maintained at 97.25% of the initial capacitance, which is obviously superior to that of $NiCo_2O_4$ after 5000 cycles, with a capacitance retention of 93%. In detail, Fig. 7b shows that the capacitance of the $NiCo_2O_4$@$NiCo_2O_4$ electrode has a small increase in the first 1200 cycles. This phenomenon should result from the fact that the capacitance fluctuates with the activation of the electrode from 1200 to 3500 cycles. After 3500 cycles, the capacitance remains relatively stable. Unexpectedly, the capacitance of the $NiCo_2O_4$ electrode decays rapidly before 500 cycles, but remains relatively stable after 500 cycles. Interestingly, the coulombic efficiency of the former electrode material is 100% after 5000 cycles. The insets are the GCD curves at the beginning of the cycle and the end of the cycle, respectively. After 5000 cycles, the GCD curve does not change much, which proves the stability of the material. Fig. 7c, d shows the SEM images of $NiCo_2O_4$@$NiCo_2O_4$ after 5000 cycles. The large sheet of the sample surface is still loaded with a large number of small sheets, which also proves the excellent mechanical properties and outstanding cycling properties of the material. The structural damage as a result of volume expansion can be alleviated by such a connected and stable structure during the cycling process.

The comparisons of the specific capacitance at a certain current density and cycling ability between the $NiCo_2O_4$@$NiCo_2O_4$ nanoflake array in our paper and other previously reported work are shown in Table 1. It can be apparently seen that the cycling performance of the fabricated composite is clearly better than that of many previously reported materials, such as $NiCo_2O_4$@$NiCo_2O_4$ nanocones (85.3% after 21000 cycles) [45], $NiCo_2O_4$@$NiCo_2O_4$ nanoflakes (83.6% after 5000 cycles) [49], Co_3O_4@$NiCo_2O_4$ nanowires (83.7% after 1500 cycles) [50], $NiCo_2O_4$@$NiCo_2O_4$ nanocacti (93.4% after 5000cycles) [51], $NiCo_2O_4$@$NiCo_2O_4$ nanoplates (90.3% after 3000cycles) [52], and $NiCo_2O_4$@NiO nanowires arrays (93.1% after 3000 cycles) [15], indicating that the electrode material made of $NiCo_2O_4$@$NiCo_2O_4$ has shown great potential in practical application. However, the specific capacitance in our work is slightly lower than that of core–shell arrays such as $NiCo_2O_4$@$NiMoO_4$ nanowires (1242 F/g at 10 mA cm^{-2}) [53], $NiCo_2O_4$@MnO_2 nanowire arrays (1471.4 F/g at 10mA cm^{-2}) [54], $NiCo_2O4$@polypyrrole nanowire arrays (1328 F/g at 2 mA cm^{-2}) [55], and $NiCo_2O_4$@$MnMoO_4$ (1705.3 F/g at 5 mA cm^{-2}) [56].

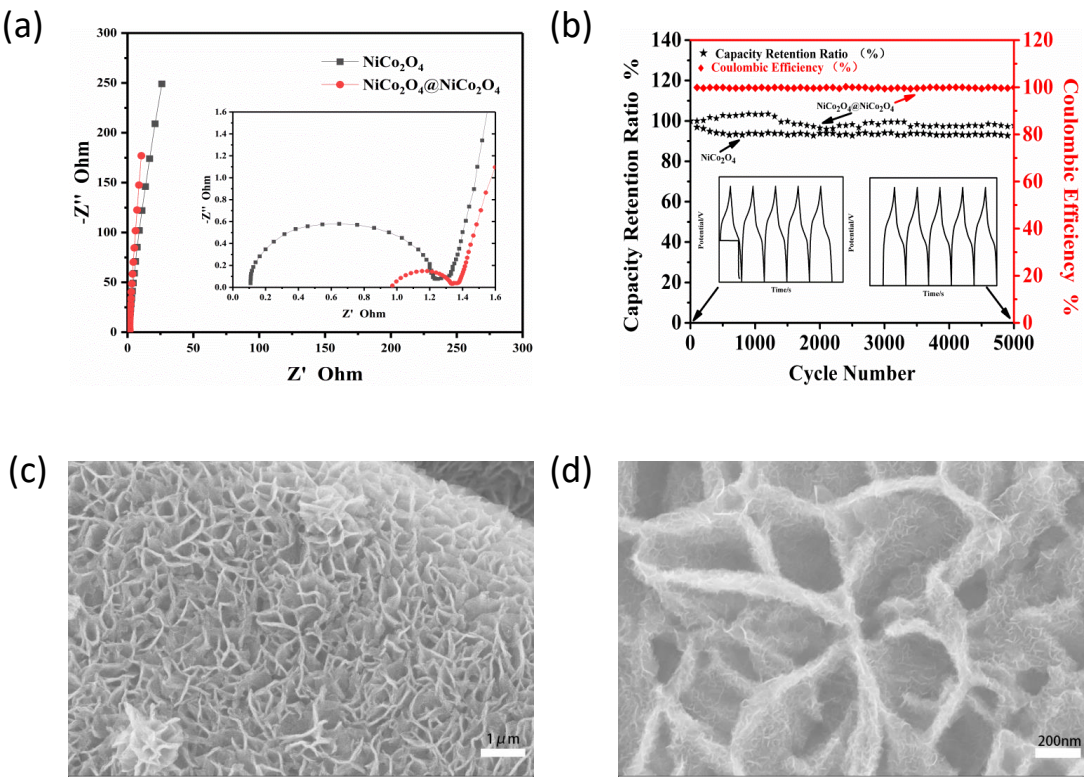

Figure 7. (a) the EIS results of $NiCo_2O_4$ and $NiCo_2O_4$@$NiCo_2O_4$.The inset from (a) presents the expanded high-frequency region of the plots. (b) Specific capacitance retention with cycle number for $NiCo_2O_4$ and $NiCo_2O_4$@$NiCo_2O_4$ and coulombic efficiency of $NiCo_2O_4$@$NiCo_2O_4$. The insets show the galvanostatic charge–discharge of $NiCo_2O_4$@$NiCo_2O_4$ at the beginning and the end of cycles. (c) and (d) SEM images of $NiCo_2O_4$@$NiCo_2O_4$ after 5000 cycles.

Table 1. The electrochemical performances of the electrode materials in our works were compared with those in other previous reports.

Materials	Specific capacitance	Rate capability	Cycling performance	Current density	Refs
$NiCo_2O_4$@$NiCo_2O_4$ nanocacti	1264 F/g at 2 A/g	64% (2-10 A/g)	93.4% (5000 cycles)	2 A/g	[51]
$NiCo_2O_4$@$NiCo_2O_4$ nanoplates	2800 F/g at 35 A/g	80% (30-75 A/g)	90.3% (3000 cycles)	50 A/g	[52]
$NiCo_2O_4$@$NiCo_2O_4$ nanocones	2045 F/g at 1 A/g	30% (1-8 A/g)	85.3% (21000 cycles)	4 A/g	[45]
Co_3O_4@$NiCo_2O_4$ nanowires	1.18 F/cm^2 at 10 mA/cm^2	67% (10-30 mA/cm^2)	85.7% （1500 cycles）	10 mA/cm^2	[50]
$NiCo_2O_4$@$NiMoO_4$ nanowires	1242 F/g at 10 mA/cm	79% (10-80 mA/cm^2)	84% (5000 cycles)	10 mA/cm^2	[53]
$NiCo_2O_4$@MnO_2 nanowires	1471.4 F/g at 10 mA/ cm^2	87% (2-20 mA/cm^2)	88% (2000 cycles)	10 mA/cm^2	[54]

$NiCo_2O4$@polypyrrole nanowires	1328 F/g at 2 mA/cm^2	80.5% (2-20 mA /cm^2)	85% (5000 cycles)	10 mA/cm^2	[55]
$NiCo_2O_4$@$MnMoO_4$ Nanocolumn	1705.3 F/ g at 5 mA /cm^2	73.5% (5-20 mA /cm^2)	92.6% (5000 cycles)	5 mA/cm^2	[56]
$NiCo_2O_4$@$NiCo_2O_4$ nanoflakes	1036 F/g at 1 A/g	69.59% (1-15 A/g)	97.25% (5000 cycles)	10 A/g	This work

4. CONCLUSIONS

Overall, we have proposed an environment-protecting and facile approach through hydrothermal calcination for preparing $NiCo_2O_4$ nanoflake arrays. The $NiCo_2O_4$@$NiCo_2O_4$ materials are synthesized in the same way by secondary growth. With the full use of a unique structure, the $NiCo_2O_4$@$NiCo_2O_4$ nanoflake array demonstrates a much higher specific capacitance and better cycling performance than of bare $NiCo_2O_4$ when applied as electrode materials in supercapacitors. Consequently, the prepared $NiCo_2O_4$@$NiCo_2O_4$ materials with remarkable electrochemical performance exhibit great development prospects for practical applications in supercapacitors or potential in electrochemical storage devices due to their simple preparation and environmental friendliness.

ACKNOWLEDGEMENTS
We are appreciative for the support from the Youth Science Fund of Northeast Petroleum University (2019QNQ-03).

References

1. J.Y. Dong , X.T. Zhang, *Appl. Surf. Sci.*, 332 (2015) 247.
2. H.Y. Fu, Z.Y. Wang, Y.H. Li and Y.F. Zhang, *Mater. Res. Innovations*, 19 (2015) S255.
3. C. Hao, S. Zhou, J. Wang, X. Wang, H. Gao and C. Ge, *Ind & Eng Chem Res*, 57 (2018) 2517.
4. X. Chen, D. Chen, X. Guo, R. Wang and H. Zhang, *ACS Appl. Mater. Interfaces*, 9 (2017) 18774.
5. L. Fan, L. Tang, H. Gong, Z. Yao and R. Guo, *J. Mater. Chem.*, 22 (2012) 16376.
6. J. Li, S. Xiong, Y. Liu, Z. Ju and Y. Qian, *ACS Appl. Mater. Interfaces*, 5 (2013) 981.
7. S. Al-Rubaye, R. Rajagopalan, S.X. Dou and Z. Cheng, *J. Mater. Chem. A*, 5 (2017) 18989.
8. W. Zhang, W. Xin, T. Hu, Q. Gong, T. Gao and G. Zhou, *Ceram. Int.*, 45 (2019) 8406.
9. J. Zhou, Y. Huang, X. Cao, B. Ouyang, W. Sun, C. Tan, Y. Zhang, Q. Ma, S. Liang, Q. Yan and H. Zhang, *Nanoscale*, 7 (2015) 7035.
10. F. Bahmani, S.H. Kazemi, Y. Wu, L. Liu, Y. Xu and Y. Lei, *Chem. Eng. J.*, 375 (2019) 121966.
11. G. Gao, H.B. Wu, S. Ding, L.M. Liu and X.W. Lou, *Small*, 11 (2015) 804.
12. D. Kong, J. Luo, Y. Wang, W. Ren, T. Yu, Y. Luo, Y. Yang and C. Cheng, *Adv. Funct. Mater.*, 24 (2014) 3815.
13. W. Li, Y. Chen, F. Li, W. Zheng, J. Yin, X. Chen and L. Chen, *Ionics*, 25 (2018) 2401.
14. Y. Li and X. Peng, *ChemistrySelect*, 2 (2017) 8959.
15. X. Liu, J. Liu and X. Sun, *J. Mater. Chem. A*, 3 (2015) 13900.

16. X. Liu, S. Shi, Q. Xiong, L. Li, Y. Zhang, H. Tang, C. Gu, X. Wang and J. Tu, *ACS Appl. Mater. Interfaces*, 5 (2013) 8790.
17. A. Chebil, O. Kuzgun, C. Dridi and M. Ates, *Ionics*,4 (2020) 864.
18. Y. Sun, W. Zhang, D. Li, L. Gao, C. Hou, Y. Zhang and Y. Liu, *J. Alloys Compd.*, 649 (2015) 579.
19. D. Li, Y. Gong, Y. Zhang, C. Luo, W. Li, Q. Fu and C. Pan, *Sci. Rep.*, 5 (2015) 12903.
20. M.C. Liu, L.B. Kong, C. Lu, X.M. Li, Y.C. Luo and L. Kang, *ACS Appl. Mater. Interfaces*, 4 (2012) 4631.
21. Y. Ouyang, R. Huang, X. Xia, H. Ye, X. Jiao, L. Wang, W. Lei and Q. Hao, *Chem. Eng. J.*, 355 (2019) 416.
22. Z. Wu, Y. Zhu and X. Ji, *J. Mater. Chem. A*, 2 (2014) 14759.
23. G. Zhang and X.W. Lou, *Adv. Mater.*, 25 (2013) 976.
24. P. Liu, Y. Liu, J. Li, M. Wang and H. Cui, *Nanoscale*, 12 (2020) 22330.
25. Y. Ding, N. Zhang, J. Zhang, X. Wang, J. Jin, X. Zheng and Y. Fang, *Ceram. Int.*, 43 (2017) 5374.
26. H. Du, Y. Li, F. Ding, J. Zhao, X. Zhang, Y. Li, R. Zhao, M. Cao, T. Yu and X. Xu, *Int. J. Hydrogen Energy*, 43 (2018) 15348.
27. Y. Wang, W. Zhang, X. Guo, K. Jin, Z. Chen, Y. Liu, L. Yin, L. Li, K. Yin, L. Sun and Y. Zhao, *ACS Appl. Mater. Interfaces*, 11 (2019) 7946.
28. H. Li, H. Xuan, J. Gao, T. Liang, X. Han, Y. Guan, J. Yang, P. Han and Y. Du, *Electrochim. Acta*, 312 (2019) 213.
29. H. Feng, S. Gao, J. Shi, L. Zhang, Z. Peng and S. Cao, *Electrochim. Acta*, 299 (2019) 116.
30. C. Chang, L. Zhang, C.W. Hsu, X.F. Chuah and S.Y. Lu, *ACS Appl. Mater. Interfaces*, 10 (2018) 417.
31. T. Zhai, L. Wan, S. Sun, Q. Chen, J. Sun, Q. Xia and H. Xia, *Adv. Mater.*, 29 (2017)527.
32. J. Mei, T. Liao, G.A. Ayoko, J. Bell and Z. Sun, *Prog. Mater Sci.*, 103 (2019) 596.
33. F. Li, Y. Xing, M. Huang, K.L. Li, T.T. Yu, Y.X. Zhang and D. Losic, *J. Mater. Chem. A*, 3 (2015) 7855.
34. X. Wang, L. Chen, S. Zhang, X. Chen, Y. Li, J. Liu, F. Lu and Y. Tang, *Colloids Surf., A*, 573 (2019) 57.
35. J. Zhi, O. Reiser and F. Huang, *ACS Appl. Mater. Interfaces*, 8 (2016) 8452.
36. T. Huang , B. Liu , P. Yang , Z .Qiu , Z .Hu, *Int. J. Electrochem. Sci.*, 13 (2018) 6144.
37. D. Guo, Y. Luo, X. Yu, Q. Li and T. Wang, *Nano Energy*, 8 (2014) 174.
38. W. Qiu, H. Xiao, M. Yu, Y. Li and X. Lu, *Chem. Eng. J.*, 352 (2018) 996.
39. Q. Wang, X. Wang, B. Liu, G. Yu, X. Hou, D. Chen and G. Shen, *J. Mater. Chem. A*, 1 (2013) 2468.
40. P. Liu, Q. Hao, X. Xia, L. Lu, W. Lei and X. Wang, *J. Phys. Chem. C*, 119 (2015) 8537.
41. H. Shi and G. Zhao, *J. Phys. Chem. C*, 118 (2014) 25939.
42. Y. Zhang, J. Wang, J. Ye, P. Wan, H. Wei, S. Zhao, T. Li and S. Hussain, *Ceram. Int.*, 42 (2016) 14976.
43. S. Hassanpoor , F. Aghely, *RSC Adv.*, 10 (2020) 35235.
44. S. Dhibar and S. Malik, *ACS Appl. Mater. Interfaces*,7 (2020) 4536.
45. X. Wang, Y. Fang, B. Shi, F. Huang, F. Rong and R. Que, *Chem. Eng. J.*, 344 (2018) 311.
46. Y.-R. Zhu, P.-P. Peng, J.-Z. Wu, T.-F. Yi, Y. Xie and S. Luo, *Solid State Ionics*, 336 (2019) 110.
47. Z. Qu, M. Shi, H. Wu, Y. Liu, J. Jiang and C. Yan, *J. Power Sources*, 179 (2019) 410.
48. C. K, N. N and K. Nagaraju, Mater. *Chem. Phys.*, 164 (2015) 98.
49. X. Chen, H. Li, J. Xu, F. Jaber, F. Musharavati, E. Zalezhad, S. Bae, K.S. Hui, K.N. Hui and J. Liu, *Nanomaterials*, 10 (2020) 1292.
50. G. Zhang, T. Wang, X. Yu, H. Zhang, H. Duan and B. Lu, *Nano Energy*, 2 (2013) 586.
51. J. Cheng, Y. Lu, K. Qiu, H. Yan, J. Xu, L. Han, X. Liu, J. Luo, J.K. Kim and Y. Luo, *Sci. Rep.*, 5 (2015) 12099.
52. Y. Anil Kumar and H.-J. Kim, *New J. Chem.*, 42 (2018) 19971.

53. Z. Gu, H. Nan, B. Geng and X. Zhang, *J. Mater. Chem. A*, 3 (2015) 12069.
54. L. Yu, G. Zhang, C. Yuan and X.W. Lou, *Chem. Commun.*, 49 (2013) 137.
55. T. Chen, Y. Fan, G. Wang, J. Zhang, H. Chuo and R. Yang, *Nano*, 11 (2016) 245.
56. C. Cui, J. Xu, L. Wang, D. Guo, M. Mao, J. Ma and T. Wang, *ACS Appl. Mater. Interfaces*, 8 (2016) 8568.